metals

MDPI

Article

Machining Distortion of Titanium Alloys Aero Engine Case Based on the Energy Principles

Zibiao Wang [1], Jianfei Sun [2,*], Wuyi Chen [2], Liangbao Liu [2] and Rongqiao Wang [1]

[1] Collaborative Innovation Center of Advanced Aero-Engine, School of Energy and Power Engineering, Beihang University, Beijing 100191, China; scientistbiao@163.com (Z.W.); wangrq@buaa.edu.cn (R.W.)
[2] Beijing Engineering Technological Research Center of High-Efficient & Green CNC Machining Process and Equipment, School of Mechanical Engineering and Automation, Beihang University, Beijing 100191, China; wychen@buaa.edu.cn (W.C.); llb1985101@163.com (L.L.)
* Correspondence: sjf@buaa.edu.cn; Tel.: +86-10-8233-9296

Received: 16 May 2018; Accepted: 14 June 2018; Published: 18 June 2018

Abstract: The simulation of a complete manufacturing process to produce an aero engine case, including forging, rolling, and machining processes, is analyzed via finite element software. The deformation of the turning and drilling processes is quantitatively studied using the energy principles. Firstly, simulations of multi-stage forging of aero engine case and machining-induced residual stress are conducted and verified via the residual stresses test in order to provide the initial elastic strain energy condition prior to machining processes. The effects of blank forging-induced residual stress and machining-induced residual stress on the deformation of titanium alloys aero engine case are investigated. Secondly, a potential energy expression for the machining processes is developed. The predicted results of turning and drilling simulations indicate that there is an optimal process in which the deformation and potential energy decline rapidly compared with the other processes and finally, gradually stabilize at the end of the process.

Keywords: titanium alloys aero engine case; multi-stage forging; energy principle; residual stresses; machining deformation prediction

1. Introduction

Titanium alloys are widely used in the aerospace industry due to their low-density, high strength, toughness corrosion resistance and good high-temperature [1]. Forging is one of the most common methods to produce blanks of shaped titanium alloy parts. However, the forgeability of titanium alloys is usually very poor, due to their narrow forging temperature range, great deformation resistance, and high strain rate sensitivity [2]. As the key component of aero engines, engine cases feature large dimensions, thin walls, low rigidity, and large material removal volume, and these features are prone to severe distortion after machining.

The blank forging induced residual stress (FIRS) and machining induced residual stress (MIRS) can deeply affect the machining deformation. Some investigations have been done to analyze the relationship between machining deformation and residual stresses, including FIRS and MIRS. Zong et al. [3] found that the influence of the cutting velocity on residual stresses lied between the cutting-edge radius and the depth of cut, which were shown to be the maximum and minimum influence factors on residual stresses, respectively. To reduce the residual stresses generated by turning ductile materials with diamond cutting tools, the optimum rake angle is about 10° and clearance angle is 6°. Young et al. [4] researched the relationship between MIRS and the corresponding machining deformation. A polynomial equation model of residual stress distribution was established by the polynomial fitting method, and the machining distortion of aluminum alloy parts was simulated by

the finite element method (FEM) and verified via experiments. The authors of that study considered that machining parameters have little influence on deformation, while tool geometry greatly impacted the MIRS. Based on the elastic theory, Nervi et al. [5] established a mathematical model to predict the machining deformation with the theory of elasticity. Both the installation position of the workpiece and the MIRS could causes relatively large deformation of the thin-walled parts. However, the main defects were that the initial residual stress of the blank as well as the material removal strategy were not considered.

Husson et al. [6] analyzed the impacts of residual stress on the machining deformation of gears. The results indicated that heat treatment ameliorates the residual stress of semi-finished products and reduces machining deformation. Huang et al. [7] proposed that the initial residual stress was the primary cause of machining deformation and that the deformation caused by MIRS accounts for about 10% of the total deformation. A machining deformation prediction model, which considered multifactor coupling effects, including the initial residual stresses, cutting loads, clamping forces, and MIRS, was established based on the FEM [8]. However, the influence of the material removal sequence was still neglected.

Brink et al. [9] investigated the manufacturing processes of gears from the aspects of blank forging and processing with heat treatment. The analyses indicated that the residual stress redistribution was the cause of the machining distortion. Brink et al. [10] proposed that processing deformation was a function of residual stress, material removal methods, and the geometry of the parts. Liu et al. [11] discussed the finite element analysis of a machining processes of a turbine disk, which was made from Inconel 718 high-temperature wrought alloy, based on the theorem of minimum potential energy. This study revealed that different orders of the material removal have different effects on the deformation and strain energy. Every other mortise broaching sequence was highly recommended for the practical production. Nevertheless, the machining induced residual stress, which has an important influence on the deformation of thin-walled parts, was not mentioned. The relationships among machining deformation, the release of elastic strain energy, and residual stress (initial and machining-induced) were unexplored.

Elastic–plastic deformation under external loads is the fundamental cause of the residual stress of forging. Since the plastic deformation will hinder the elastic recovery after the removal of external loads, the residual stress is generated by the incongruous deformation. The plastic deformation produces heat energy which quickly dissipates into the parts and the surroundings, while the elastic deformation is stored in the workpiece as the elastic strain energy that gives parts a metastable state. The stock removal process breaks the self-equilibrium of the metastable state such that the release of the elastic strain energy leads to strain redistribution and the deformation of parts. Finally, the balance is reached in the minimum potential energy state. The refore, the storage and release of strain energy are the root causes of the deformation of workpieces with residual stresses.

The flow chart of the methodology in this paper mainly includes four activities, shown in Figure 1. Firstly, part 1 describes the complete manufacturing processes of an aero engine case based on FEM, including the forging, rolling, and heat treatment processes. Secondly, the simulation of machining-induced residual stress is conducted and verified via the residual stress test. Thirdly, predictions of the deformation and strain energy caused by MIRS and FIRS are made at different stages of the material removal. Fourthly, the simulations are verified via experiments. The key points of this study are that the different orders of the material removal have different effects on the deformation and the strain energy. Finally, an optimal process route that can effectively control the processing deformation is obtained.

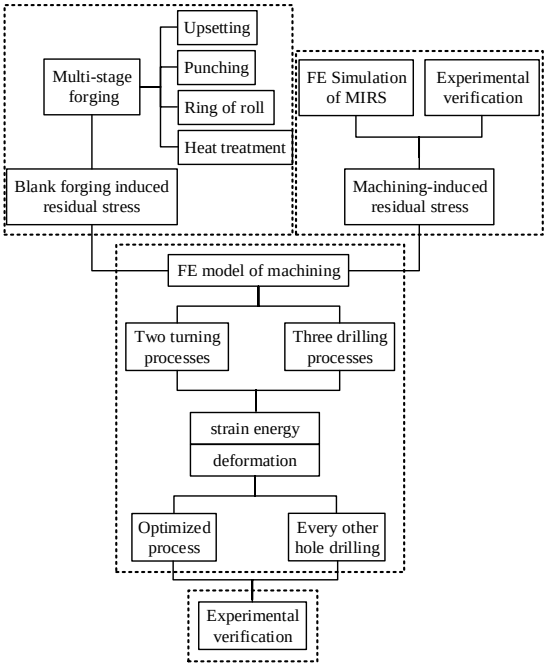

Figure 1. Flow chart of the methodology.

2. Multi-Stage Forging Finite Element Simulation

The material used was the titanium alloy, Ti–6Al–4V. According to research related to the forgeability of Ti–6Al–4V, the beta transus temperature of the alloy is 980 °C, and its chemical composition is shown in Table 1. Higher temperatures cause the material to exhibit β-brittleness, while lower temperatures bring about increased deformation resistance and surface cracks. Repeated axial upsetting and drawing can refine the as-cast microstructure under a temperature in the (α + β) phase region and β phase transition region [12,13]. The residual stress is closely related to the parameters of forging process. Its Young's modulus is 110 GPa and Poisson's ratio is 0.34. The Arrhenius constitutive equation has widely been used to describe the relationship among the flow stress, strain rate, and temperature.

$$\dot{\varepsilon} = A[sinh(\alpha\sigma)]^n exp\left(-\frac{Q}{RT}\right), \quad (1)$$

where σ is the flow stress (MPa); $\dot{\varepsilon}$ is the strain rate (s^{-1}); T is the temperature (K); R is the universal gas constant (8.325 $J{\cdot}mol^{-1}{\cdot}K^{-1}$); and Q is the activation energy of hot deformation ($K{\cdot}J{\cdot}mol^{-1}$). A, n, and α are the material constants which are calculated by the same procedure under different deformation strains [2].

Table 1. Chemical composition of Ti–6Al–4V (mass fraction, %).

Al	V	O	Fe	C	N	H	Ti
6.08	4.19	0.11	0.06	0.009	0.005	0.002	Bal.

Forging the blank of an engine case includes three steps: upsetting, punching and rolling. The DEFORM was applied to simulate the multi-stage forging of the aero engine case. The workpiece model was elasto-plastic. The friction coefficient of the contact surface was 0.5 [14]. The dies were rigid body. The temperature of the environment was 20 °C. Specifically, the heat transfer coefficients at

the workpiece–die and workpiece–air interfaces were set to 1 N/s/mm/°C and 0.02 N/s/mm/°C, respectively. The initial temperature was 1020 °C [15,16].

Considering the axisymmetric geometrical characteristics of the aero engine case, a 2D axisymmetric finite element (FE) model was created with four-node quadrilateral elements as the initial billet to be forged and punched. The compression speed of upsetting was 2 mm/s. The initial height of the workpiece was 180 mm. The final height of the workpiece was 130 mm. The strain is illustrated in Figure 2. In addition, the inputs of residual stress, strain, and temperature for punching were extracted from the solutions of the upsetting simulation. As shown in Figure 3, the punching process included two steps. The diameter of the first punching was 100 mm; the second one was 150 mm. The velocity of punching was 100 mm/s. The stress concentration occurred in the shear plane. With respect to the rolling process, the simulation was converted into a three-dimensional format due to the non-axisymmetry in loading and boundary, as shown in Figure 4. The meshes of the FE model were tetrahedral elements. At the beginning of the process, the rotational speeds of the driving roll, mandrel, guide roll and axial roll were 2 rad/s, 4.72 rad/s, 6.67 rad/s, and 6 rad/s, respectively. The compression speed of the mandrel was 0.2 mm/s. Due to the constant volume condition and the hypothesis of the ring contour approximate circle in rolling, the diameter of the ring began to increase as the thickness of the ring decreased. The motion of the guide rolls and the rotational speed of axial rolls in radial-axial ring rolling were previously derived by Li et al. [17]. The complex mechanical forces and thermal effect for hot forging determined the FIRS. It is a coupled field that includes the interactive effects of distortion, heat transfer, and heat generated from plastic deformation. The heat treatment process was divided into two parts: holding for 1–2 h at 800 °C and then air cooling [18]. The mechanical and thermal properties are fully provided in the material library in DEFORM (V11.0, SFTC, Columbus, OH, USA).

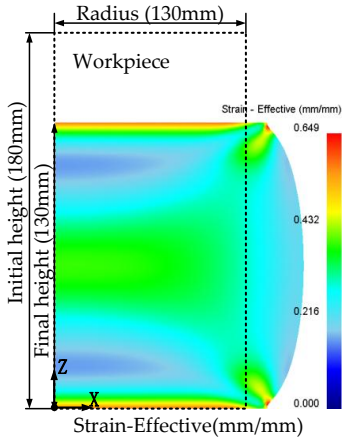

Figure 2. Dimensions and equivalent strain during upsetting.

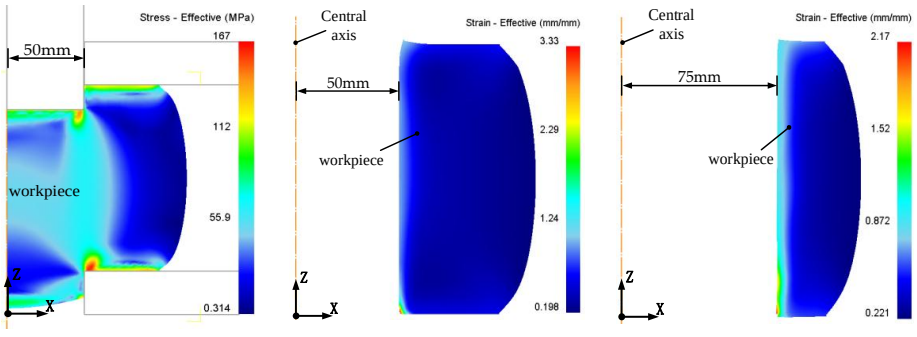

(**a**) Punching (**b**) First punching (**c**) Second punching

Figure 3. Stress and strain during punching.

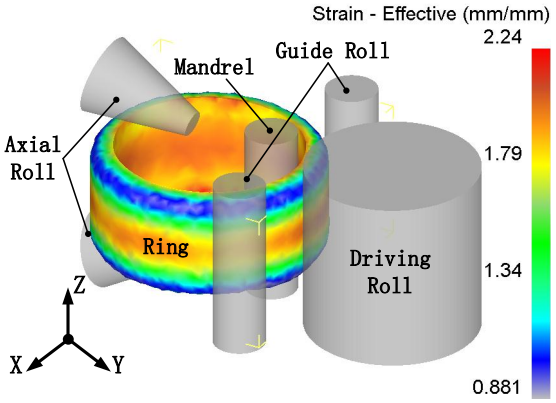

Figure 4. Rolling finite element model.

Figure 5 reveals that the temperature of in the center of the workpiece was higher than on the surface. This mainly resulted from the varied values of heat transfer and plastic deformation from the surface to the center. The rmal stress was the main component of residual stress, and the temperature gradient was the cause of thermal stress. Deformation resulting from upsetting was broken up into three areas, as shown in Figure 6. The metal in area I had the most difficulty flowing among the three areas owing to its low temperature, the hindrance of the surrounding materials, and a friction force between the workpiece and die which was presented in Figure 2. Area II had the most plastic deformation as well as a weak heat transfer, so the temperature was the highest.

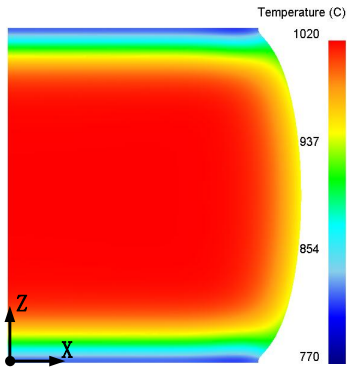

Figure 5. Temperature of the upsetting.

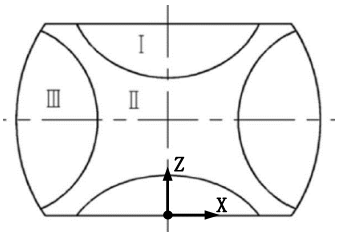

Figure 6. Classification of the deformation area.

The ring-rolling residual stress profile was nearly linear along the radial direction because the surface temperature fell faster than the inner temperature during the air cooling process. The inner and outer radii of the ring were 103.4 and 131.4 mm, respectively. The surface of the outer circle generated compressive residual stress and the surface of the inner circle generated tensile stress, as shown in Figure 7. The stress data from ten points was extracted. The distribution of the residual stress of

ring-rolling was drawn from the first point (P1) to the tenth point (P10), as shown in Figure 8. There was asymmetric distribution of the axial and tangential stresses in the radius direction. The maximum stresses were 56.9 and 38.9 MPa, respectively. The radial stress component was very small at all times; its maximum value was 5.5 MPa.

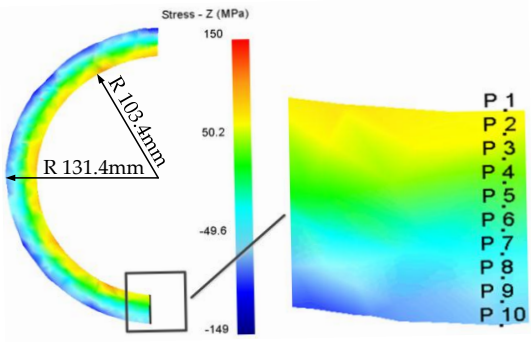

Figure 7. Ring-rolling residual stress from air-cooling.

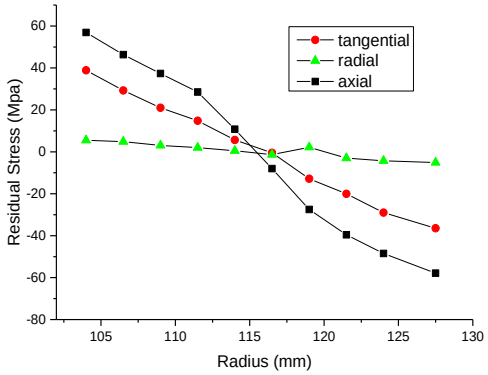

Figure 8. Ring-rolling residual stress along the radial direction.

3. Turning-Induced Residual Stress

3.1. FE Simulation of Turning-Induced Residual Stresses

The cutting tool parameters are shown in Table 2. The distribution of the turning-induced residual stress was analyzed with AdvantEdge software (V5.1, Third Wave Systems, Minneapolis, MN, USA), as shown in Figures 9a and 10a. The meshes of the FE model were triangular elements. The immersed cooling method was applied. The coolant temperature was 20 °C. The heat transfer coefficient was 10^4 W/(K·m^2). As illustrated in Figures 9b and 10b, the distribution of the MIRS was approximately V type, and the maximum stress was at a depth of 50 μm. The turning-induced residual stress was 150 μm deep. The maximum compressive stresses in the feed direction and cutting direction were −332.4 and −466.9 MPa, respectively, during the outside diameter (OD) turning process. During internal diameter (ID) turning, the maximum absolute values of compressive stress in the feed direction and cutting direction at 50 μm were 283.3 and 386.4 MPa, respectively.

Table 2. Tool parameters.

Insert	Machining Position	Material	Rake Angle	Clearance Angle	Nose Radius	Cutting Edge Radius
CCGX120408-ALH10	Outside diameter (OD) turning and facing	Carbide	20°	7°	0.8 mm	0.02 mm
CCMT120408-MM1125	Internal diameter (ID) turning	Carbide	7°	7°	0.8 mm	0.02 mm

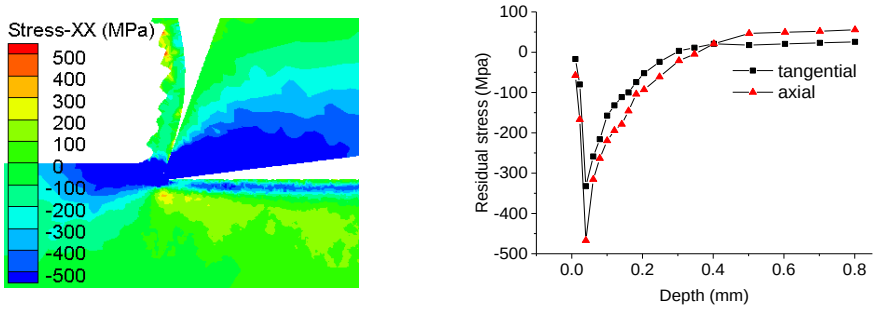

(**a**) Simulation Stress (**b**) Machining-induced residual stress varying with depth

Figure 9. Residual stress after OD turning.

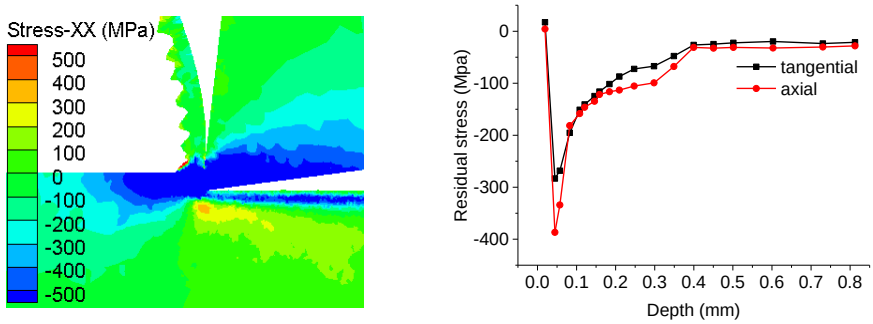

(**a**) Simulation Stress (**b**) Machining-induced residual stress varying with depth

Figure 10. Residual stress after ID turning.

3.2. Experimental Verification for Turning-Induced Residual Stress in the FE Simulation

In the previous section, a simulation of turning-induced residual stress was conducted. In this section, we describe the measurement of residual stress experimentally. Prism (Stresstech Oy, Jyväskylä, Finland) was applied to measure the residual stress. It combined the tried-and-true hole-drilling method with digital imaging and electronic speckle pattern interferometry (ESPI). The arrangement was illustrated in Figure 11. The instrument delivered the complete planar stress state [19]. The technique utilized a stress relaxation technique, in which a small hole was drilled into the part, thereby removing residual stress and causing a rebalancing of the residual stresses. This led a slight surface distortion which was measured optically using ESPI. The typical application for Prism is stress depth profile measurements by incremental drilling [20–23].

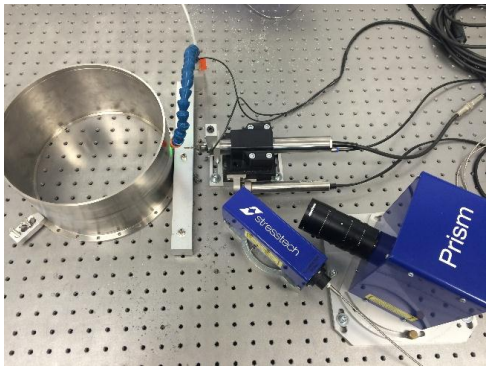

Figure 11. Residual stress measurement arrangement.

It was evident that the radial stress was too small to measure by simulation. So, the test only measured the tangential and axial stresses. The authors selected five measuring positions on the circumference in order to exclude accidental error. The results of the five measurements showed a similar trend. The compressive stress area was from 0–200 μm, and the stress gradient was large. However, some errors were very large, especially those within 200 μm. This might have been caused by unstable factors such as vibration, inhomogeneous material organization, and measuring device error. As observed in Figure 12, when the process was complete, a double V-shaped distribution curve of residual stress induced by the machining was obtained. The first V-shaped curve was from 0–150 μm; the second one was from 150–300 μm. The deeper layer stress was generated during blank making. This occurred because the cutting edge was not perfectly sharp. Some of the cutting material was pressed into the machined surface due to cutting edge roundness and tool flank, which is a complex deformation process. When the newly produced surface escaped from the tool flank, the elastic deformation could not release completely, owing to the constraint of the plastically-deformed surface and therefore, produced highly compressive residual stress. The cutting heat was mostly generated from the distortion of the chip and the friction at the tool–chip and tool–work interfaces, so the cutting temperature was very high because the temperature of inner material fell slowly, but the surface temperature fell rapidly causing uneven thermal expansion and the machine surface-generated residual tensile stress. The refore, it was the coupling effect of the elastic–plastic deformation and cutting temperature that produced the machining residual stress. The maximum absolute values of the compressive stress in the feed direction and cutting direction at 50 μm were 278 and 445 MPa, respectively, during the OD turning process. The stress curve trends of the OD turning process, both simulated and measured, were similar. The depth of residual stress was 150 μm with a large stress gradient. Moreover, the errors of the maximum residual stress were 35.4 and 8.7 MPa. However, the simulated and measured stresses differed greatly at the same depth. This might have been caused by the boundary conditions, such as ignoring the tool wear and vibration during experiment, and because the friction model was simplified into coulomb friction in the simulation.

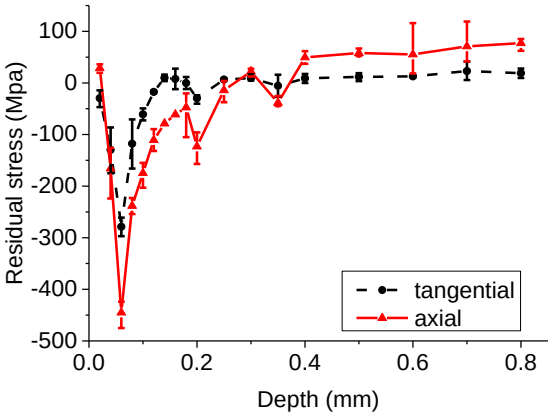

Figure 12. Machining-induced residual stress.

4. FE Simulation for the Machining of an Aero Engine Case Based on the Minimum Potential Energy Theory

4.1. Principle of Minimum Potential Energy in the Theory of Elasticity

It is assumed that thermal energy is neither generated nor lost during elastic deformation. The total potential energy, Π_p, is the sum of the elastic strain energy, U, stored in the deformed body and the work, W, done by external loads, associated with the applied surface forces and body forces [24]:

$$\Pi_p = U + W, \tag{2}$$

$$U = \int_v \overline{U} dV = \int_v \frac{1}{2}\left(\sigma_x \varepsilon_x + \sigma_y \varepsilon_y + \sigma_z \varepsilon_z + \tau_{xy}\gamma_{xy} + \tau_{xz}\gamma_{xz} + \tau_{yz}\gamma_{yz}\right) dV, \quad (3)$$

$$W = -\int_{S_T} T_i u_i dS_T - \int_V F_i u_i dV, \quad (4)$$

where $\overline{U}$ is the strain energy density function; σ and τ are normal and shear stresses; ε and γ are normal and shear strains; V is the volume of the part; T_i is the ith component of the surface traction; u_i is the ith component of the deformation; F_i is the ith component of a body force; and S_T is areas where the tractions are applied.

The minimum total potential energy principle asserts that a structure or a part shall deform or displace to a certain location that minimizes the total potential energy. This position is stable at equilibrium. The elastic strain energy in the blank of an aero engine case is developed during the forging process (the inharmonic elastic–plastic deformation of metal) and the machining process (large elastic–plastic deformation and high cutting temperature gradient beneath the machined surface). When all external loads, T_i and F_i, have disappeared after unloading, the total potential energy, Π_p, left within the machined aero engine case is solely comprised of the strain energy:

$$\Pi_p = U + U', \quad (5)$$

where U' is the machining-induced strain energy.

Before the machining process, the total strain energy of the blank is stable. During the machining process, the equilibrium is broken due to material removal. On one hand, the total strain energy will reduce. On the other hand, the workpiece will be deformed to another new state of static balance. In addition, the integral results of the internal stresses through the whole workpiece will be close to 0. The theory is based on the hypothesis that the total potential energies are equal during the process.

$$\Pi_{pi-1} = \Pi_{pi} + U_{ie}, \quad (6)$$

where Π_{pi} and Π_{pi-1} represent the potential energy before and after machining in step i. The U_{ie} stored in the chips is removed.

The impact of MIRS on the workpiece is described using the machining-induced strain energy to total strain energy ratio. The ratio is η_i after machining in step i:

$$\eta_i = \frac{U_i'}{U_i}. \quad (7)$$

When more allowance is removed as chips, the initial strain energy, U_i is reduced, but the machining-induced strain energy, U_i' increases. Accordingly, η_i increases and U' has more influence on the workpiece.

4.2. Modeling and Simulation for Machining of an Aero Engine Case

4.2.1. The Blank and Finished Part

The blank and the finished part of the aero engine case are illustrated in Figures 13 and 14. The forging of the engine case blank included three steps: upsetting, punching, and rolling. The machining of the part had two processes: turning (OD, ID, and facing) and drilling. The dimension of the blank was 118 mm in height and 208 mm and 255 mm in ID and OD. The engine case wall thickness was 2 mm. Almost ninety percent of blank material was removed. The right-handed X(r)-Y(θ)-Z cylindrical system was used, with the X-direction through the radius, the Y-direction around the circumference of workpiece, and the Z-direction along the height.

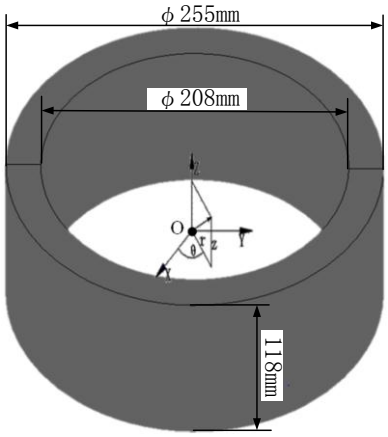

Figure 13. Blank of aero engine case.

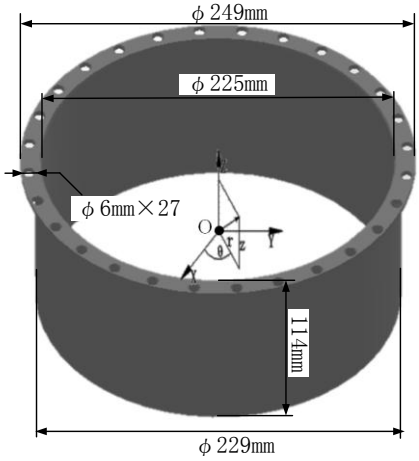

Figure 14. Aero engine case.

4.2.2. FE Model and Boundary Conditions

During the turning process, the part geometry, machining load, clamping condition, etc., were Z-axis symmetric. Accordingly, a 2D axisymmetric analysis model was adopted to investigate a radial section of the engine case. The model was able to reduce the calculation time and memory use effectively. The drilling model was changed from two-dimensional into three-dimensional because of the non-axisymmetry in the drilling process. The initial strain energy was extracted from the forging in txt format and was then read into the FE model. The central points of the model were selected, and all degrees of freedom were constrained in order to prevent the movement of rigid parts [25]. During the simulation of machining, the removal of material was realized through the concept of element death. During the machining process, the equilibrium was broken by material removal. The workpiece was distorted to another static balance [26,27].

In following chapters, the effects of MIRS and FIRS on the deformation and PE are presented. A comparative analysis for the deformation and PE in the different processes is conducted.

4.3. Simulation Results and Discussion

4.3.1. Turning Process

Further study was focused on the deformation and PE variation during turning. During the simulation of machining, the allowance to be removed was separated into ten zones at a radial section

of the blank, as illustrated in Figure 15. Nine zones were removed. The remainder of workpiece was the aero engine case.

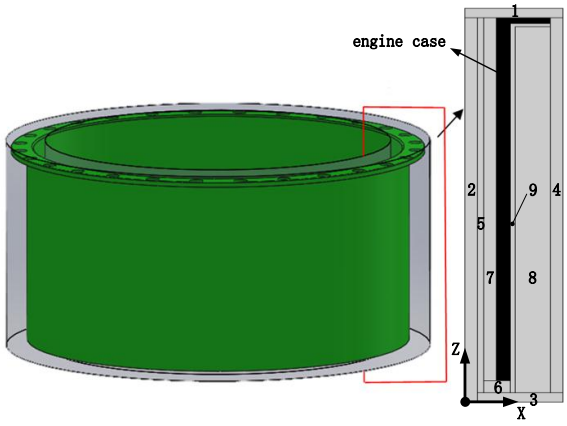

Figure 15. Radial section of the blank (The order of material removal was 1-2-3-4-5-6-7-8-9).

In the machining process, the material removal resulted in the release of residual stress and strain. The different sequences of the material removal had different effects on deformation [11]. The refore, there could be an optimal process, in which the FIRS and strain energy show faster release during rough machining compared with other processes. In other words, when the material removal volume is equal in different process strategies, the optimal process will produce the largest reduction in strain energy.

In the FE simulation, FIRS and MIRS were applied to the model. The FIRS was asymmetrically distributed in the radius direction. The surfaces of the outer circle generated compressive residual stress and the inner circle generated tensile stress, as shown in Figure 8. A layer of MIRS was generated in the machining process. The thickness of each layer was 150 μm. The stress distribution was detailed in Section 3. The strain energy and deformation were obtained by FEM.

During the simulation of machining, the original process (the order of material removal was 1-2-3-4-5-6-7-8-9) and the optimized process (1-2-3-4-8-9-5-6-7) were compared. Figures 16a–d and 17a–d present the total deformation of the part as the proportion of material removed varied, which provides beneficial information for studying the effect of strain energy in removed material on the distortion. To further investigate the relationship between strain energy and part distortion in the turning simulation, the maximum deformation was selected as the research object. Figure 18 presents the maximum deflection and strain energy as a function of the removal sequences. The solid curve represents the effect of FIRS on the deflection and strain energy without MIRS. The dash line represents the deflection and strain energy with FIRS and MIRS during the original process. The dash-dot line represents the deflection and strain energy with FIRS and MIRS after optimized processing. As illustrated in Figure 18a, at the beginning of the material removal, the first material removed (Zones 1 & 2) was the upper end and inner circle of the ring respectively. The total deformation increased with the growth of material removal; meanwhile, the deflection reached a maximum value of 0.051 mm after removing Zone 2. The removal of tensile stress Zone 2 resulted in the deformation of the ring. In the optimized process, when the compressive stress in Zones 4, 8 and 9 was removed, reverse deformation resulted, so that the deformation of the ring decreased from 0.051 to 0.025 mm. The results are shown in Figure 17b,c. As shown in Figure 17d, the distortion was stable at the end of the process (i.e., Zones 5, 6 and 7), which eventually reached 0.021 mm. For the original process, the removal of tensile stress Zones 5, 6 and 7 occurred prior to the machining of compressive stress Zones 8 and 9, as shown in Figure 16c,d, so the deformation suddenly dropped down to 0.021 mm at the end of the turning (i.e., Zones 8 & 9). The sudden decrease at the end of the process would have badly disturbed the deformation control, since no sufficient allowance could be removed to

correct the form error. Thus, the optimized process firstly cut away the zones of compressive residual stress from the workpiece and then removed the zones of tensile residual stress, which was better for deformation control.

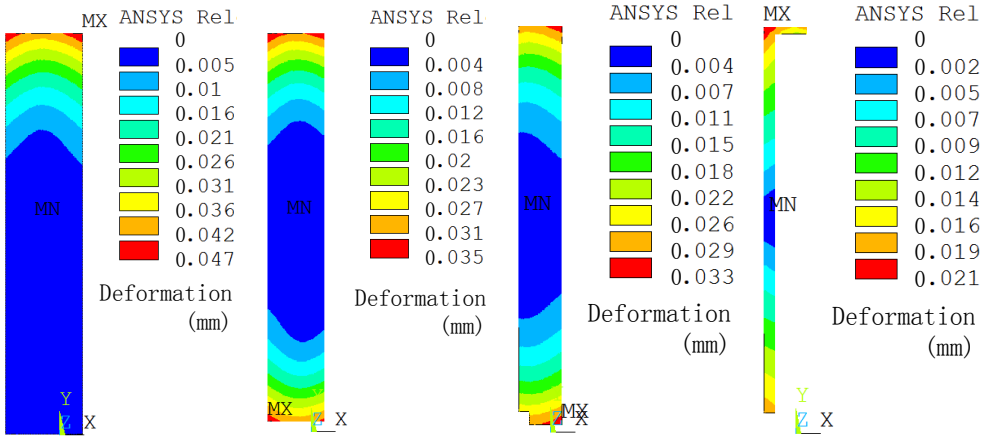

(**a**) Zone 1 removed (**b**) Zone 4 removed (**c**) Zone 7 removed (**d**) Zone 9 removed

Figure 16. Maximum distortion during material removal in the original process.

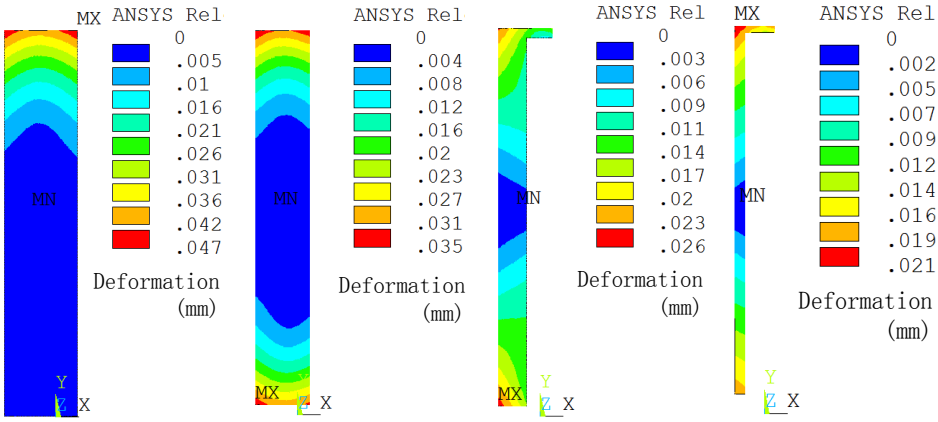

(**a**) Zone 1 removed (**b**) Zone 4 removed (**c**) Zone 9 removed (**d**) Zone 7 removed

Figure 17. Maximum distortion during material removal in the optimized process.

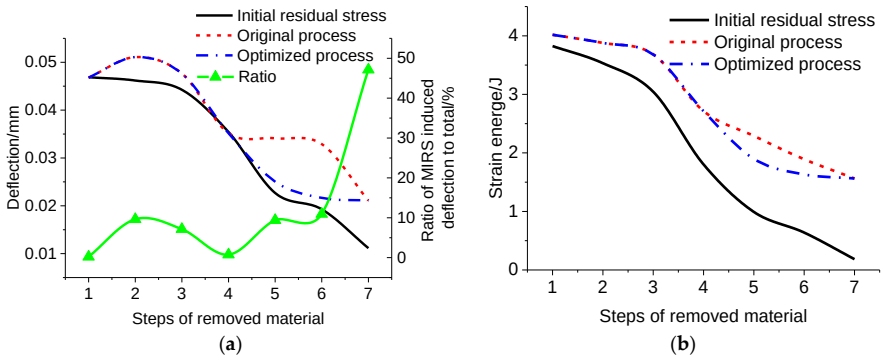

Figure 18. Deformation (**a**) and strain energy (**b**) varying with material removal.

As shown in Figure 18a, the solid line with triangles stands for the ratio of MIRS-produced deformation to the total deformation. In the beginning (i.e., Zones 1 and 2), the material removal added

to the newly finished surface. The layer of MIRS was generated in the finished surface. So, the ratio climbed to 9.6% with the growth of material removal. The machining of Zones 3 and 4 induced by MIRS resulted in reverse deformation compared with Zones 1 and 2. The refore, the ratio decreased. When more material was removed, the workpiece stiffness reduced. The MIRS-induced deformation increased, but the total deformation decreased. Consequently, the ratio reached 47.1% at the end of process. The refore, FIRS and MIRS significantly affect deformation. In the beginning of process, the FIRS played a leading role. Along with the decrease in the stiffness of the workpiece, the MIRS gradually became the dominant effect.

In terms of strain energy, the total potential energy, Π_p, was the sum of the initial strain energy within the forging blank of an aero engine case, U_i, and the machining-induced strain energy, U_i', stored in the deformed body. The strain energy obtained via FEM was the minimum potential energy in each process. Specifically, in the beginning (i.e., Zone 1 to Zone 3), the strain energy in the remaining material slowly dropped. During the optimized process, when the material from Zones 4 and 8 was removed, there was a rapid decline in strain energy. However, in the final stage (Zone 5 to Zone 7), the Π_p declined slightly. The strain energy in the original process showed a slower decrease compared with the optimized process. The re is a downside to this: the more strain energy the workpiece stored, the more unstable the workpiece became. So, when the material removal volume was equal, the storage of less strain energy in the workpiece symbolized a better optimized process. The strain energy of the optimized process remained below the original process from the fifth to the seventh step. So, the optimized process was better than the original one.

As illustrated in Figure 18b, the difference between the two curves (the solid curve and the dash-dot one) was the machining-induced strain energy (U_i'). As material removal increased, the initial strain energy, U_i, was reduced, but U_i' increased. According to Equation (7), η_i increased when there was a rise in the volume of material removal. In other words, the more material removed, the larger the ratio of machining-induced strain energy to total strain energy. As illustrated in Figure 18, the curves of deformation and strain energy were very alike.

In regard to the deformation and strain energy, their fluctuation and stability were two important factors used to judge the quality of the processes. The machining process included seven steps, as illustrated in Figure 18. The average differences in the adjacent data points for the two processes are listed in Table 3. The optimized average difference was 31% of the original average difference from the fifth to seventh step. The refore, for the optimized process, the deformation was more stable at the end of the process which would benefit the deformation control.

Table 3. The average differences between the adjacent data points.

Processes	Whole Process (μm)	From Fifthth to Seventh Step (μm)
Original process	5.7	6.5
Optimized process	5.7	2.0

4.3.2. Drilling Process

Three processes were simulated. The deformation of the parts is illustrated in Figure 19. The holes on the flange were drilled with three drilling processes, consisting of sequent drilling, symmetric drilling, and every other hole drilling (see Table 4). The variation in the total strain energy and deformation between the three drilling processes are illustrated in Figures 20 and 21. For the drilling process, the relative variation in strain energy and deformation was small, owing to the low material removal volume. Among the three processes, every other hole drilling caused a larger decrease in strain energy with the growth of material removal, and then, the three strain energy values were equal at the end of the process. The distortion of sequent and symmetric drilling seemed stable at the beginning of the processes. However, the distortion suddenly swung at the end of the process. The distortion of every other hole drilling was lower than the other ones at the end of process. For the

three processes, the average reduction in relative strain energy is listed in Table 5. The value of every other hole drilling was lower than the other ones from the 14th to 27th drilling. The refore, every other hole drilling was sufficient for precision finishing.

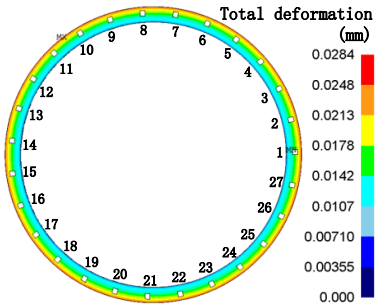

Figure 19. Deformation during drilling.

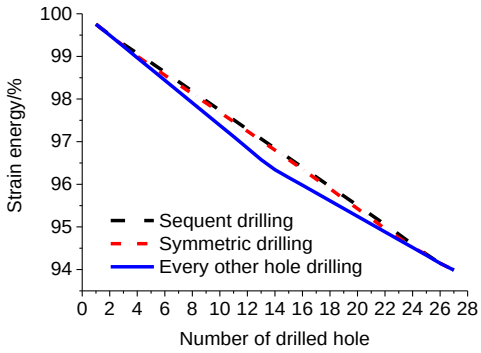

Figure 20. Variation in strain energy with amount of drilling.

Table 4. Variations in deformation and strain energy with different drilling processes.

Sequent Drilling Process			Symmetric Drilling Process			Every Other Hole Drilling Process		
No. Hole	Deform-Ation (mm)	Strain Energy/%	No. Hole	Deform-Ation (mm)	Strain Energy/%	No. Hole	Deform-Ation (mm)	Strain Energy/%
1	0.029272	99.755	1	0.029272	99.755	1	0.029272	99.755
2	0.029286	99.512	3	0.02927	99.492	14	0.029276	99.496
3	0.029293	99.289	5	0.029288	99.249	2	0.029273	99.235
4	0.029294	99.072	7	0.029287	99.005	15	0.029272	98.968
5	0.02929	98.854	9	0.029305	98.782	3	0.029273	98.704
6	0.029287	98.632	11	0.029304	98.559	16	0.029274	98.440
7	0.029286	98.408	13	0.029321	98.342	4	0.029272	98.176
8	0.029286	98.183	15	0.029319	98.125	17	0.029269	97.911
9	0.029287	97.960	17	0.02933	97.907	5	0.029284	97.647
10	0.029288	97.736	19	0.029326	97.688	18	0.029293	97.383
11	0.0292885	97.513	21	0.029323	97.468	6	0.029253	97.119
12	0.029289	97.290	23	0.029321	97.247	19	0.02912	96.851
13	0.029288	97.067	25	0.02932	97.024	7	0.028923	96.578
14	0.029286	96.844	27	0.029316	96.802	20	0.028827	96.343
15	0.029283	96.620	2	0.029316	96.576	8	0.02884	96.157
16	0.029282	96.396	4	0.029288	96.353	21	0.028839	95.979
17	0.029293	96.173	6	0.029289	96.122	9	0.028837	95.796
18	0.029311	95.949	8	0.029227	95.896	22	0.028837	95.613
19	0.029322	95.726	10	0.029227	95.660	10	0.028838	95.430
20	0.029319	95.504	12	0.029121	95.429	23	0.028838	95.248
21	0.029291	95.283	14	0.029121	95.194	11	0.028835	95.065
22	0.029229	95.058	16	0.028962	94.958	24	0.028839	94.883
23	0.029123	94.827	18	0.028963	94.750	12	0.028856	94.700
24	0.028963	94.590	20	0.028748	94.515	25	0.028826	94.519
25	0.028749	94.355	22	0.028749	94.355	13	0.028761	94.334
26	0.02858	94.147	24	0.02858	94.147	26	0.02858	94.147
27	0.028375	93.987	26	0.028375	93.987	27	0.028375	93.987

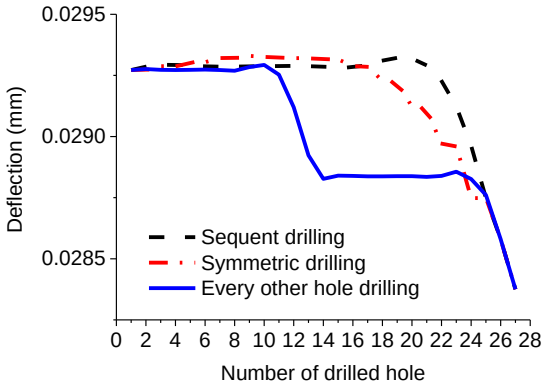

Figure 21. Deformation varying with amount of drilling.

Table 5. The average reduction in relative strain energy between the drilling holes.

Drilling Processes	Before Drilled 14th Hole (%)	After Drilled 14th Hole (%)
Sequent drilling	0.224	0.220
Symmetric drilling	0.227	0.217
Every other hole drilling	0.263	0.181

5. Experimental Verification of the Deformation Simulation

A turning-milling machining center KMC800 UMT made by KEDE (Dalian, China) was used for the machining of an aero engine case made of Ti–6Al–4V titanium alloy. The cutting parameters are listed in Table 6. The aero engine case was machined with the optimized process, as shown in Figure 22. The radial run-out and flatness were obtained by the radial deformation and Z-direction deformation of FE simulation, respectively. The experimental values were measured by a dial indicator. The flatness errors of the mounting face and the outer circular run-out for both the simulation and the experiment are shown in Table 7. The relief and redistribution of the residual stress were the primary causes of the deformation of parts with weak rigidity. According to the results of the simulated optimization process, when the compressive stress in Zones 4, 8 and 9 were removed, the distortion gradually became stable until the end of process. At that moment, the deformation error was theoretically eliminated, owing to reconstruct datum in the experiment. The refore, the simulation results were larger than the experimental values.

Table 6. Cutting parameters.

Cutting Parameter	Rough Machining	Finish Machining	Drilling
v_c m/min	48	80	26
f mm/r	0.1	0.08	0.04
a_p mm	2	0.2	

Table 7. Deformation in the experiment and the simulation.

Reseach Methods	Flatness (mm)	Radial Runout (mm)
Experiment	0.02	0.02
Simulation	0.027	0.022

Figure 22. Machining process.

6. Conclusions

In this paper, the complete manufacturing process of an aero engine case including forging, rolling, heat treatment, and machining was analyzed with FEM. Meanwhile, the effects of FIRS and MIRS on the deformation were quantitatively investigated by using the energy principles in the different processes. The optimized process was used in experiments, respectively. The main conclusions drawn were as follows:

1. The ring-rolling residual stress profile was nearly linear along the radial direction. The surfaces of the outer circle generated compressive residual stress and the inner circle generated tensile stress. The distribution of the MIRS was approximately V type with a maximum depth of 150 μm. The maximum absolute values of the compressive stresses in the feed direction and cutting direction at 50 μm were 278 and 445 MPa, respectively.
2. During the early stages of the process, FIRS played a leading role in the deformation and strain energy. FIRS-induced deformation accounted for about 90% of the total deformation of the component. As the stiffness of the workpiece decreased, the MIRS gradually became the dominant effect. MIRS-induced deformation accounted for about 47.1% of the total deformation at the end of the process.
3. During turning, the deformation or strain energy of the optimized process reduced rapidly in the early stages compared with the other processes. Finally, they gradually became stable at the end of the process. The fluctuation in the amplitude of deformation in the optimized process accounted for 31% of the original process at the end of the process. Moreover, the results indicated that the optimized process could allow better deformation control.
4. During the drilling, among the three plans, the strain energy from every other hole drilling declined more sharply as the amount of removed material increased compared with the other two processes. Meanwhile, the deformation was controlled more easily than in the other two processes.

Author Contributions: Z.W., W.C., R.W. and J.S. conceived and designed the experiments; Z.W. and L.L. performed the experiments; Z.W. and J.S. analyzed the data; Z.W. and W.C. wrote the paper.

Funding: This research was funded by National Major Science and Technology Project of China [Grant Number 2017ZX04011009]

Acknowledgments: The authors would like to thank Jiangzhen Guo for his assistance in improving the content and figures. The authors would also like to thank the support of National Major Science and Technology Project of China [Grant Number 2017ZX04011009].

Conflicts of Interest: The authors declare no conflict of interest.

References

1. Williams, J.C.; Starke, E.A. Progress in structural materials for aerospace systems. *Acta Mater.* **2003**, *51*, 5775–5799. [CrossRef]
2. Peng, X.; Guo, H.; Shi, Z. Constitutive equations for high temperature flow stress of TC4-DT alloy incorporating strain, strain rate and temperature. *Mater. Des.* **2013**, *50*, 198–206. [CrossRef]
3. Zong, W.J.; Li, D.; Cheng, K.; Sun, T.; Liang, Y.C. Finite element optimization of diamond tool geometry and cutting process parameters based on surface residual stresses. *Int. J. Adv. Manuf. Technol.* **2007**, *32*, 666–674. [CrossRef]
4. Young, K.A. Machining-Induced Residual Stress and Distortion of the Thin Parts. Ph.D. Thesis, Saint Louis Washington University, Louis, MO, USA, 2005.
5. Nervi, A.S. Mathematical Model for the Estimation of the Effects of Residual Stresses in Aluminum Plates. Ph.D. Thesis, Saint Louis Washington University, Louis, MO, USA, 2005.
6. Husson, R.; Dantan, J.Y.; Baudouin, C. Evaluation of process causes and influences of residual stress on gear distortion. *CIRP Ann. Manuf. Technol.* **2012**, *61*, 551–554. [CrossRef]
7. Huang, X.; Sun, J.; Li, J. Finite element simulation and experimental investigation on the residual stress-related monolithic component deformation. *Int. J. Adv. Manuf. Technol.* **2015**, *77*, 1035–1041. [CrossRef]
8. Tang, Z.T.; Yu, T.; Xu, L.Q.; Liu, Z.Q. Machining deformation prediction for frame components considering multifactor coupling effects. *Int. J. Adv. Manuf. Technol.* **2013**, *68*, 187–196. [CrossRef]
9. Brinksmeier, E.; Lübben, T.; Fritsching, U. Distortion minimization of disks for gear manufacture. *Int. J. Mach. Tools Manuf.* **2011**, *51*, 331–338. [CrossRef]
10. Brinksmeier, E.; Sölter, J.; Grote, C. Distortion Engineering—Identification of Causes for Dimensional and Form Deviations of Bearing Rings. *CIRP Ann. Manuf. Technol.* **2007**, *56*, 109–112. [CrossRef]
11. Liu, L.; Sun, J.; Chen, W.; Zhang, J. Finite element analysis of machining processes of turbine disk of Inconel 718 high-temperature wrought alloy based on the theorem of minimum potential energy. *Int. J. Adv. Manuf. Technol.* **2016**, *88*, 3357–3369. [CrossRef]
12. Guo, P.; Zhao, Y.; Zeng, W. The effect of microstructure on the mechanical properties of TC4-DT titanium alloys. *Mater. Sci. Eng. A* **2013**, *563*, 106–111. [CrossRef]
13. Pei, C.; Li, Z.; Ding, J. Influence of Forging Processing on Dynamic Properties of TC4 Titanium Fan Blade. *Rare Met. Mater. Eng.* **2017**, *46*, 118–123.
14. Deng, K.; Huang, M.H.; Lu, X.J. Real-time modeling method of deformation force in whole forging process. *J. Cent. South Univ. (Sci. Technol.)* **2014**, *11*, 3778–3785.
15. Ducato, A.; Buffa, G.; Fratini, L.; Shivpuri, R. Influence of Geometrical Ratios in Forgeability of Complex Shapes during Hot Forging of Ti-6Al-4V Titanium Alloy. *Procedia Eng.* **2014**, *81*, 516–521. [CrossRef]
16. Lim, T.; Pillinger, I.; Hartley, P. A finite-element simulation of profile ring rolling using a hybrid mesh model. *J. Mater. Process. Technol.* **1998**, *80–81*, 199–205. [CrossRef]
17. Li, S.; Liu, D.; Ma, Y. Calculation Method of Guide Roll Locus in Radial/Axial Ring Rolling. *Chin. J. Hot Work. Technol.* **2010**, *11*, 48–52.
18. Li, C.; Ma, J. *Chinese Materials Engineering Dictionary-Nonferrous Metal Materials Engineering*; Chemical Industry Press: Beijing, China, 2006; ISBN 9787502573287.
19. Gao, H.; Zhang, Y.-D.; Wu, Q. Experimental Investigation on the Fatigue Life of Ti-6Al-4V Treated by Vibratory Stress Relief. *Metals* **2017**, *7*, 158. [CrossRef]
20. Steinzig, M.; Upshaw, D.; Rasty, J. Influence of Drilling Parameters on the Accuracy of Hole-drilling Residual Stress Measurements. *Exp. Mech.* **2014**, *54*, 1537–1543. [CrossRef]
21. Benedetti, M.; Fontanari, V.; Winiarski, B. Residual stresses reconstruction in shot peened specimens containing sharp and blunt notches by experimental measurements and finite element analysis. *Int. J. Fatigue* **2016**, *87*, 102–111. [CrossRef]
22. Schajer, G.S.; Steinzig, M. Dual-Axis Hole-Drilling ESPI Residual Stress Measurements. *J. Eng. Mater. Technol.* **2010**, *132*, 011007. [CrossRef]
23. Ponslet, E.; Steinzig, M. Residual Stress Measurement Using the Hole Drilling Method and Laser Speckle Interferometry Part II: Analysis technique. *Exp. Tech.* **2003**, *27*, 17–21. [CrossRef]
24. Preissner, E.C.; Vinson, J.R. Application of theorem of minimum potential energy to a complex structure part I: Two dimensional analysis. *Int. J. Solids Struct.* **2003**, *40*, 1089–1108. [CrossRef]

25. Liu, L.; Sun, J.; Chen, W. Study on the machining distortion of aluminum alloy parts induced by forging residual stresses. *Proc. Inst. Mech. Eng. Part B J. Eng. Manuf.* **2015**, *4*, 618–627. [CrossRef]
26. Wang, Z.; Chen, W.; Zhang, Y. Study on the Machining Distortion of Thin-walled Part Caused by Redistribution of Residual Stress. *Chin. J. Aeronaut.* **2005**, *18*, 175–179. [CrossRef]
27. Gao, H.; Zhang, Y. An analytical model for predicting the machining deformation of a plate blank considers biaxial initial residual stresses. *Int. J. Adv. Manuf. Technol.* **2017**, *93*, 1473–1486. [CrossRef]